

Influence of Temperature and Pressure on the Wetting Progress in 21700 Lithium-Ion Battery Cells: Experiment, Model, and Lattice Boltzmann Simulation

Johannes Wanner,^{*[a]} Matthias Burgard,^[a] Nabih Othman,^[a] Soumya Singh,^[a] and Kai Peter Birke^[a, b]

The electrolyte filling and subsequent wetting of the active material is a time-critical process in the manufacturing of lithium-ion batteries. Due to the metallic cell housing, the process phenomena are insufficiently accessible, preventing the replication of the wetting processes by mathematical or simulative methods and hindering efforts to accelerate the wetting process. Therefore, this publication employs a glass cell housing for electrolyte filling of a 21700 cylindrical cell to investigate the wetting at different temperatures and process

pressures. In parallel, a mathematical replication of the wetting, as well as a lattice Boltzmann pore-scale simulation, is used to evaluate the influence of these varying process boundary conditions. The results show a strong temperature dependence on electrolyte wetting and the positive effect of pressure changes in the wetting process. These findings are particularly relevant to the process design of large-scale cylindrical cell manufacturing.

Introduction

The lithium-ion cell is used in a wide spectrum of applications in a diversity of formats.^[1,2] A major development goal in battery technology is to reduce cell costs and the CO₂ footprint of the cell.^[3] This can be achieved for all cell formats, particularly by reducing process times and the amount of material required.^[4,5] The filling of the liquid electrolyte into the dry battery materials and the subsequent wetting during cell assembly is a process with significant potential for reducing process time and resources.^[5,6] Therefore, various methods for investigating and accelerating the process are discussed in the literature for all cell formats.^[7–9] For cylindrical cells, there is limited knowledge of how the electrolyte is distributed within the cell and its cavities, as the metallic housing represents a barrier for optical investigations.^[10] This complicates a mathematical replication and the possibilities to positively influence the wetting process.^[11] Kaden et al. provide an overview of various methods to investigating the wetting process:^[12] These methods include optical techniques such as the capillary rise test, droplet spread, X-ray or neutron spectroscopy, and electrical methods such as

impedance spectroscopy and chronoamperometry. Optical methods such as the capillary rise test or droplet spread are used at the material level to investigate wetting with high resolution and good sampling frequency.^[12,13] Davoodabadi et al. use the droplet spread test to investigate the electrolyte movements at the electrode level with different electrolytes and electrolyte temperatures. However, the transferability of these results to the cell level is not established.^[14] Electrical and optical X-ray or neutron radiography methods are used at the cell level, but these provide poor spatial and limited temporal resolution of wetting. These limitation hinder efforts to accelerate wetting process: For instance, Knoche et al. observed two different process pressures using neutron radiography in a pouch cell. However, the effect on the resulting wetting progress falls within the fluctuation range of the measurement method.^[15] The results are further mathematically fitted, which prevents transferability to other process pressures and framework conditions. Günter et al. also consider the framework conditions to transfer the mathematical replication to different process temperatures and ambient pressures. This is validated with neutron radiography measurement of a prismatic cell and fitting by an effective pore radius and a tortuosity value, generalized to the cell level. Here, the temporal and spatial resolution is also a major obstacle to investigating the effects of wetting within the cell layers.^[16] In Hagemeister et al. a larger cell model is coupled with a pore model and wetting is investigated at different electrolyte temperatures and process pressures.^[17] Combining experiments with a pore scale cell model achieves a useful resolution. In Hagemeister et al., wetting is investigated at different electrolyte temperatures and process pressures.^[17] A large number of simulation studies are also known in the literature, but these are mainly dedicated to the electrode and material design of the battery cell.^[18–22] The lattice Boltzmann method (LBM) is mainly used to investigate

[a] J. Wanner, M. Burgard, N. Othman, S. Singh, Prof. Dr. K. P. Birke
Fraunhofer Institute for Manufacturing Engineering and Automation IPA,
Nobelstrasse 12, 70569 Stuttgart, Germany
E-mail: johannes.wanner@ipa.fraunhofer.de

[b] Prof. Dr. K. P. Birke
Institute for Photovoltaics, Chair of Electrical Energy Storage Systems,
University of Stuttgart Pfaffenwaldring 47, 70569 Stuttgart, Germany

 Supporting information for this article is available on the WWW under
<https://doi.org/10.1002/batt.202400531>

 © 2024 The Authors. *Batteries & Supercaps* published by Wiley-VCH GmbH.
This is an open access article under the terms of the Creative Commons Attribution License, which permits use, distribution and reproduction in any medium, provided the original work is properly cited.

wetting at the pore level. Variations in the boundary conditions, apart from the electrode geometry, are generally limited to the contact angle or viscosities, without accounting for varying process conditions.^[23,24] Moreover, the combination of high-resolution experimental investigation, mathematical replication, and simulation comparisons is not extensively documented in the literature for this problem.^[25]

Additionally, product and process fluctuations result in different boundary conditions for wetting, leading to varying wetting durations.^[7] Areas of unwetted active material in the battery cell reduce capacity, which is compensated by increasing the quantity of electrolyte and extending wetting times.^[15,26] This ultimately leads to more expensive cells and lower energy density.

To address these issues, this publication employs a special glass cylindrical cell housing to observe wetting on the outermost winding. An estimation of the wetting of the inner windings was carried out in previous work.^[10] The transparency of the glass housing allows for the mathematical reproduction of the wetting progress, and, supported by a pore-scale simulation, enables the evaluation methods to accelerate wetting. This includes the influence of temperature and variations in ambient pressure.

Theory of Capillary Wetting

In porous media, the Lucas–Washburn equation and its various extensions are used to describe the capillary rise.^[27,28] Capillary pressure P_C dominates the wetting process. Additionally, the loss of viscosity described by Darcy's law (∇P_V) is a significant influencing factor. The hydrostatic pressure (P_H) of the liquid and the ambient gas pressure (p_0) also play an important roles. The relationships can be described as follows:^[27,28]

$$\frac{dh}{dt} = \frac{\sum P}{8\mu h} (r_{\text{eff}}^2), \text{ with : } \sum P = P_C - P_H - \nabla P_V - p_0, \quad (1)$$

where h represents the liquid penetration height, and μ is the liquid's dynamic viscosity. In porous media with variable pore radii, an effective pore radius r_{eff} is defined. The capillary pressure P_C is given by:

$$P_C = \frac{2\gamma\cos(\theta)}{r_{\text{eff}}}. \quad (2)$$

Where γ is the surface tension between the liquid and the gas, and θ is the contact angle between the liquid, gas, and solid surface. The hydrostatic pressure of the liquid is defined as:

$$P_H = g \cdot \rho \cdot h \cdot \sin(\psi), \quad (3)$$

where ρ represents the liquid density, g is the acceleration due to gravity, and ψ is the alignment angle of the porous media relative to the horizontal axis. The viscous pressure loss ∇P_V of the liquid is defined by

$$\nabla P_V = \frac{\mu \cdot dh/dt \cdot h}{k}, \quad (4)$$

where k describes the permeability of the porous media.^[28] The equation can be summarized for open porous media:

$$\frac{dh}{dt} = \frac{r_{\text{eff}}^2 k}{h(8k\mu + \mu r_{\text{eff}}^2)} \cdot \left[\frac{2\gamma\cos(\theta)}{r_{\text{eff}}} - \rho \cdot g \cdot h \cdot \sin(\psi) \right]. \quad (5)$$

Methods

Experimental Setup

The experiments are designed in two-stages. First, as in previous publications, the separator and electrode are stacked and pressed in a defined manner.^[10,29] This setup allows for high resolution observation of wetting using a glass plate and the capillary rise method. The stack extends below the glass plates to facilitate initial wetting. To initiate the wetting process, 1 ml of DMC or PC is applied to the glass plate below the electrode stack for each experiment.

The experimental setup is then scaled up to the cell level. For this purpose, the battery materials are wound into a 21700-format jelly roll using an industrial winding machine. The jelly roll is placed in a special glass housing that matches the dimensions of a metallic 21700-cell housing. The battery cell is a developed in-situ cylindrical cell, especially for the observation of electrolyte wetting. The wetting process is activated by a defined quantity of electrolyte and an injection device at the upper end of the jelly roll's winding core.

In both cases, the setup is illuminated and recorded by an industrial camera, DFK 33GX183 from The Imaging Source, LLC (Charlotte, NC, USA), with a sample rate of two frames per second and a resolution of 20 megapixels. The pressure and ultrasonic experiments are conducted at a temperature of 20°C. For data evaluation, the recorded pictures are processed using Matlab R2024a to increase sharpness, contrast, and gray values, allowing for the quantification of the wetting level: The wetted separator is significantly darker compared to the unwetted separator. As soon as the hue value of the image pixel exceeds the value 140 of 255, this pixel is considered to be wetted. In the observed area, the lowest wetted pixel is taken as the reference value for the respective image.

Materials

A graphite anode and a Celgard 2500 separator are used for the capillary rise test experiments, based on previous work.^[10] The materials are examined using the Keyence VK-9710 laser scanning microscope (Keyence, Osaka, Japan) and are characterized by their porosity, grain diameter, and pore sizes, as detailed in Table 1. The graphite anode is illustrated in Figure 1. The permeability values are derived from previous work.^[10]

Different materials are utilized for the experiments on the jelly roll scale: NMC cathodes are employed for the vacuum tests, while LFP cathodes are used for the temperature tests.

For wetting, the electrolyte solvents dimethyl carbonate (DMC) and propylene carbonate (PC) sourced from Sigma-Aldrich (St. Louis, MO, USA), are used in the capillary rise tests, both are central components of lithium-ion battery electrolytes. The material properties of DMC include surface tension ($\gamma = 32.01 \cdot 10^{-3}$ N/m), dynamic viscosity ($\mu = 1.464 \cdot 10^{-3}$ Pa · s), and density

	anode	separator
coating thickness	90 μm	25 μm
porosity	25 %	55 %
grain diameter	2.89 μm	275–321 nm
pore radius	957 nm	275 nm
permeability k	$2.86 \cdot 10^{-14} \text{ m}^2$	$5.2 \cdot 10^{-15} \text{ m}^2$
contact angle θ	14.6°	32°

($\rho = 1070 \text{ kg/m}^3$). The properties of PC are as follows: surface tension ($\gamma = 45.75 \cdot 10^{-3} \text{ N/m}$), dynamic viscosity ($\mu = 8.248 \cdot 10^{-3} \text{ Pa} \cdot \text{s}$), and density ($\rho = 1204 \text{ kg/m}^3$). These values, are based on the manufacturer's specifications and literature references.^[24,30–33] DMCs is used for the temperature tests conducted at the cell level. For pressure experiments, a special electrolyte with a minimal dye tracing content from E-Lyte Innovations GmbH is employed. The contact angles are determined using an optical contact angle measurement and contour analysis system, the OCA 40 from Data Physics Instruments GmbH (Filderstadt, Germany).

Pore Model Setup

The LBM pore model simulation examines the effective pressure-wetting behavior and the movement of gas bubbles under different boundary conditions. The simulation is conducted in the open-source environment Palabos.^[34] The setup is adopted from previous work and parameterized according to the graphite anode material described in Table 1.^[10,25,29] The parameters are adjusted to the respective boundary conditions and are listed in Supporting Information Tables 3 and 4. The simulation results are evaluated using ParaView 5.11 and Matlab R2024a, with one voxel of a lattice unit corresponding to 45.9 nm.

Based on the microscopy image of the anode, a 2D geometry is extracted for the simulation. A gray filter converts the surface's graphite particles into a binary 2D image, resulting in a electrode geometry with dimensions of $66.1 \times 20.4 \mu\text{m}^2$, as shown in Figure 1.

The pressure-saturation simulation is conducted in the y-direction. The two fluids, ρ^E and ρ_{dis}^G , are specified as boundary conditions. First, the geometry is defined with gas density ρ^G and electrolyte density ρ_{dis} . The contact angles are set using the adhesion parameters $G_{\text{ads,wetting}}$ for the electrolyte, and $G_{\text{ads,non-wetting}}$ for the

gas, applying like a bounce-back condition. A y-force on the gas represents the difference in density between the gas and the liquid. Wetting occurs due to the pressure difference between the fluid densities, the interaction parameter G_{inter} , and the time step Δt .^[23,35]

$$P = \frac{1}{3} \left[\rho + \rho_{\text{dis}} \right] + \frac{1}{3} \left[G_{\text{inter}} \cdot \rho \cdot \rho_{\text{dis}} \cdot \Delta t^2 \right], \quad (6)$$

$$\Delta P = P_{\text{inlet}} - P_{\text{outlet}}. \quad (7)$$

Where ΔP corresponds to the capillary pressure and is enhanced by an external force applied in the y-direction at layer $y=1$. This force is increased by 1000 N every 250 time steps. A lattice cell is wetted if the gas density drops below $\rho^G < 1 \text{ mu/lu}^3$ and thus the liquid prevails at this lattice cell. The saturation degree is defined as the ratio of wetted lattice cells to all gas-filled lattice cells at the beginning of the simulation. In addition to observing the capillary rise of the electrolyte in the porous media, the dynamics of gas entrainment is also examined. To this end, a gas bubble with a 550.8 nm diameter is placed in an electrolyte environment in a geometry section. An external force also stimulates the movement of the gas bubble through the pore, according to Ref. [36,37]. To achieve this, the force applied in the positive y-direction to the lattice cells filled with electrolyte is increased by 10 N every 250 iterations in the simulation.

Results

Influence of Process Temperature

Variations in ambient temperature (T) is a common method influencing wetting. This temperature control affects the density, surface tension, and viscosity of the electrolyte.^[31,38,39] For the DMC solvent used, this results in the following Equations:

$$\rho(T) = -1.3673 \cdot T + 1470.8, \quad (8)$$

$$\mu(T) = 6.195 \cdot 10^{-8} \cdot T^2 - 4.637 \cdot 10^{-5} \cdot T + 8.8 \cdot 10^{-3}, \quad (9)$$

$$\gamma(T) = -1.447 \cdot 10^{-4} \cdot T + 7.1482 \cdot 10^{-2}. \quad (10)$$

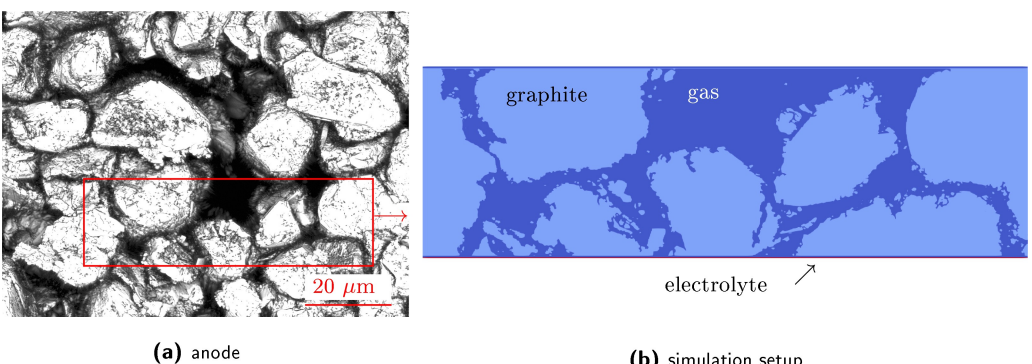


Figure 1. Microscopy image of the used graphite anode (a) and the resulting simulation setup (b).

The surface tension of the liquid (γ_{liquid}), directly influences the contact angle between the liquid, gas, and solid:^[40]

$$\cos(\gamma) = \frac{\gamma_{\text{solid}} - \gamma_{\text{liquid-solid}}}{\gamma_{\text{liquid}}}. \quad (11)$$

Experiments

To experimentally assess the effects of these parameter changes, the solvent is tempered to 5 °C and 45 °C, and 1.5 ml is injected into the 21700 cell. This volume is less than the required electrolyte of the active material. It is chosen to fill the jelly roll core and the cavities beneath it. Additional electrolyte is injected after the initial wetting phase.

The observed wetting process is illustrated in Figure 2, where a change in contrast of the outermost separator indicates the progression of wetting. At both electrolyte temperatures, wetting occurs from the lower part of the jelly roll to the top. Initially, the wetting is very heterogeneous, depending on how the electrolyte contacts the material. Additionally, the adhesive strip stabilizing the jelly roll decelerates the wetting process. Particularly at 50 s and 45 °C, the separator below the adhesive strip is wetted from below, the sides, and from above. This area becomes completely wetted after 210s, posing a significant risk of gas entrainment. An electrolyte increase between the jelly roll and the housing can be observed between 250 – 1350 s at 45 °C, indicated by particularly bright areas. The ongoing

electrolyte rise inside the jelly roll reduces this effect. After 350 s, a uniform horizontal distribution of the electrolyte in the cell can be observed at both temperatures, followed by a further uniform increase in wetting height. Overall, faster wetting is observed at 45 °C compared to 5 °C. To quantify the exact wetting progress, the lowest wetting height visible in each picture is plotted over time in Figure 3a.

The optical findings from Figure 2 are confirmed here. Initially, a rise in wetting to 3 mm (5 °C) and 5 mm (45 °C) due to the cell housing and the injection is recorded. After initial wetting, the wetting height increases to a maximum height of 18.7 mm of the adhesive strip in 255 s. From 260 s onward, an acceleration of the minimum wetting height is noticeable at 45 °C, which leads to the slower wetting of the separator under the adhesive strip. Subsequently, faster wetting occurs. After 500 s, a minimum wetting height of 42 mm is reached. A similar progression is noted for the 5 °C experiment, though with slower wetting from the beginning. Particularly, a deceleration in wetting is seen from 310 s, followed by a rapid rise at 340 s, caused by gas entrapment between the separator and the adhesive strip. From 350 s onward, a faster increase in wetting is evident, though it is slower than at 45 °C. After 500 s, a total wetting height of 25 mm is recorded. Achieving the wetting height of 18.7 mm took 34.6% faster in the experiment at 45 °C than at 5 °C.



Figure 2. Experimental results of wetting the cylindrical cell at $T=5^{\circ}\text{C}$ and $T=45^{\circ}\text{C}$. The LFP jelly roll is fixed with two green adhesive tapes and placed in the glass cell housing. After injecting 1.5 ml of solvent into each cell, wetting occurs at different speeds from bottom to top.

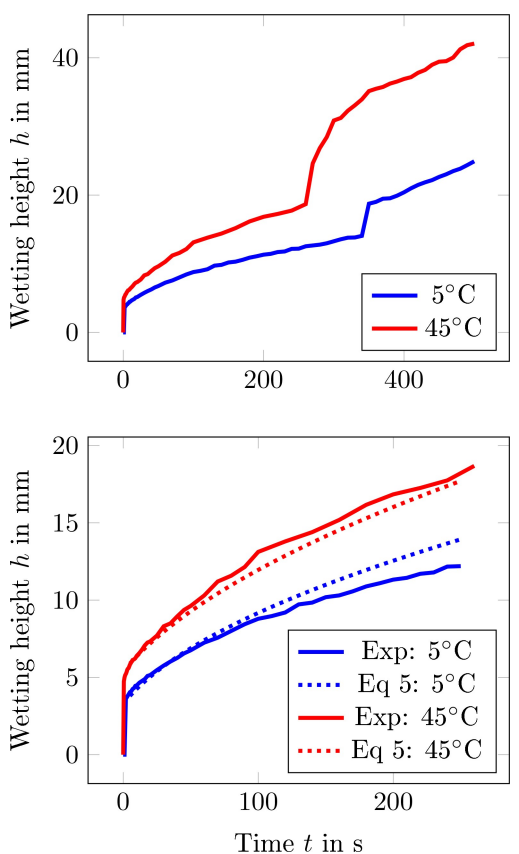


Figure 3. Plot of the wetting height of the cylindrical cell at 5 °C and 45 °C over time. The figure includes both the experimental wetting data and the calculated replication of the wetting represented by dashed lines.

Mathematical Replication

The experiments are replicated using Equation 5, with the initial condition set as the wetting height observed in the experiments. An effective pore radius of $r_{\text{eff}} = 40 \text{ nm}$ and a permeability of $k = 5.2 \cdot 10^{-15} \text{ m}^2$ are assumed for both temperatures. The density, surface tension, contact angle, and viscosity are calculated according to Equations 8 to 11 for the respective temperatures. To exclude the influence of gas entrapment in the experiments, only the wetting data up to 250 s in Figure 3b is considered. The calculated wetting heights accurately match the experimental results in both cases. At 5 °C, a discrepancy is observed where the calculated wetting height exceeds the experimental wetting data from 180 s, likely due to gas entrapments. With consistent boundary conditions, the wetting height of 65 mm is reached at 5830 s for 5 °C and 3790 s for 45 °C. This indicates a 35% faster wetting rate at 45 °C compared to 5 °C, aligning with experimental findings. If the pore radius and permeability of the anode from Table 1 are assumed, the calculated wetting times to achieve a 65 mm wetting height are significantly reduced to 1170 s for 5 °C and 760 s for 45 °C. This reduction confirms that the wetting process at 45 °C is 35% faster, regardless of the pore radius and permeability.

Pore Model Results

To evaluate the effects of different process temperatures on the wetting process, the LBM pore model simulation is parameterized with the varying density, surface tension and viscosity constants from Equations 8 to 9, and Tables 3 and 4. The contact angle is defined by the adhesion coefficient G_{ads} and is set individually for each simulation. Furthermore all specified conversion factors, apart from the length change for different temperatures. As the y-force is increased equally for the defined time steps for all simulations, this value is also set individually for different temperatures. The geometry depicted in Figure 1b is employed for the simulation, and the results are presented in Figure 4. Wetting occurs at varying capillary pressures. At 45 °C, wetting begins at 210 kPa, followed by an increase in wetting. However, no further wetting process is observed beyond a capillary pressure of 342 kPa. In contrast, a lower temperatures, higher capillary pressures are required to initiate and accomplish wetting of the geometry. For example, at 5 °C, wetting starts at 728 kPa, and no further wetting occurs beyond 1.43 MPa. Across all simulations, a gas entrapment of 6.86% is visible in the geometry due to consistent geometric boundary conditions. Consequently, a lower electrolyte temperature requires a higher capillary pressure to initiate wetting. This observation aligns with Equation 2, which accounts for temperature-dependent surface tension and, contact angles while maintaining the same capillary radius. The results indicate that a temperature increase from 5 °C to 15 °C significantly reduces the required capillary pressure, demonstrating that higher temperatures lower, the capillary pressure required for wetting.

Since gas entrapments considerably affect wetting, the movements of gas bubbles, particularly their rise as a function of temperature, is investigated through simulation. For this purpose, the section shown in Figure 1, is parameterized with temperature dependent factors, as depicted in Figure 5. Initially, the gas bubble is located at the bottom of the geometry and is pushed upward by the increasing force in the y-direction. Figure 5a illustrates an example of a gas bubble stuck in a pore at a height of 68 pixels. Figure 5b shows the positions of the

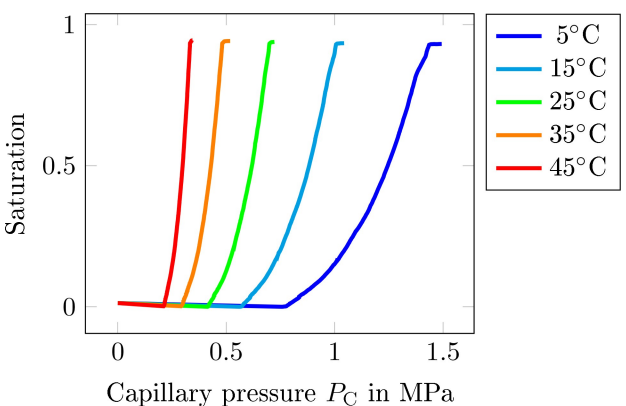


Figure 4. Results of the pore model simulation of electrolyte saturation over capillary pressure for different electrolyte temperatures.

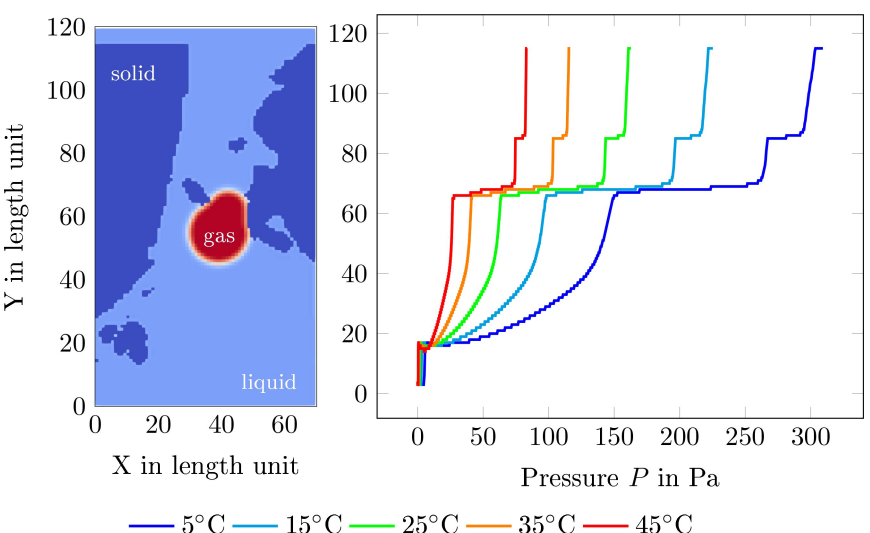


Figure 5. The setup of the gas bubble rise is illustrated on the left. One length unit corresponds to 45.9 nm. On the right, the temperature-dependent rise through the geometry is depicted with the corresponding required pressure.

gas bubble as a function of the applied force at different temperatures. The pressure-rise characteristics of the gas bubble match to the capillary pressure characteristics from Figure 4. The gas bubble overcomes the barrier at 68 pixels at pressure of 73.2 Pa at 45°C, up to 262 Pa at 5°C. This demonstrates that gas bubbles rise more easily at higher temperatures with lower pressures. An increase in temperature from 5°C to 15°C has a significantly greater effect on the required pressure than an increase from 35°C to 45°C. This correlation can be applied to reduce gas entrapments in the cell's wetting process.

Influence of Process Pressure

Applying process pressure to the wetting process in a porous media has various effects: First, the cell or experiment design plays a significant role. In the cylindrical cell, shown in Figure 6,

process pressure is applied to the interface between the electrolyte and air, both inside and outside the porous media.

If the ambient pressure remains stable, the pressure inside and outside the porous media equalizes at label 6 ($\sum = p_0 - p_0$). However, with dynamic pressure variations, the ambient pressure directly affects the interface outside the porous medium. Inside the porous media, the process gas experiences a pressure gradient through the porous medium according to Equation 4, resulting in an imbalance that influences the wetting process at label 6 ($\sum = p_0 - (p_0 - \nabla P_V)$). In this context, it is not the wetting height of the porous medium that is relevant, but rather the height of the material that remains unwetted. According to Ref. [41], changes in ambient pressure affects the liquid's surface tension. Simultaneously, temperature variations modify the contact angle changes per Equation 11. If a similar linear relationship to that found in Ref. [41] is applied to the solvents DMC and PC, based on $\gamma_{1bar,DMC} = 14.6^\circ$, the contact angle changes to $\gamma_{0.1bar,DMC} = 15.1^\circ$ and $\gamma_{6bar,DMC} = 7.7^\circ$.

Material Level

The effects of different process pressures on wetting are investigated and evaluated experimentally. All experiments were conducted at 20°C. As shown in Figure 7, three tests are performed at different process pressures. These include a reference at ambient pressure (0.968 bar). The pressure P_1 starting at 20 mbar and increases from $t=25$ s to ambient pressure by $t=210$ s. In contrast, pressure test P_2 reaches 900 mbar by $t=174$ s, followed by a subsequent reduction of the pressure to 20 mbar by $t=490$ s. The wetting heights exhibit a simultaneous progression by $t=25$ s. After this, wetting for P_1 and P_2 proceeds in parallel but faster than at P_{amb} until $t=210$ s. Subsequently, the wetting of P_1 slows relative to P_2 , aligning with the wetting height of P_{amb} by $t=$

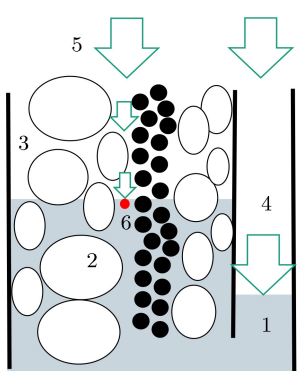


Figure 6. The application of the process pressure on the electrolyte (1) inside and outside the porous media (2) is illustrated. (3) represents the unwetted areas, (4) shows the free areas outside the medium, (5) indicates the airflow and (6) denotes the contact point at the interface between electrolyte, pore, and gas.

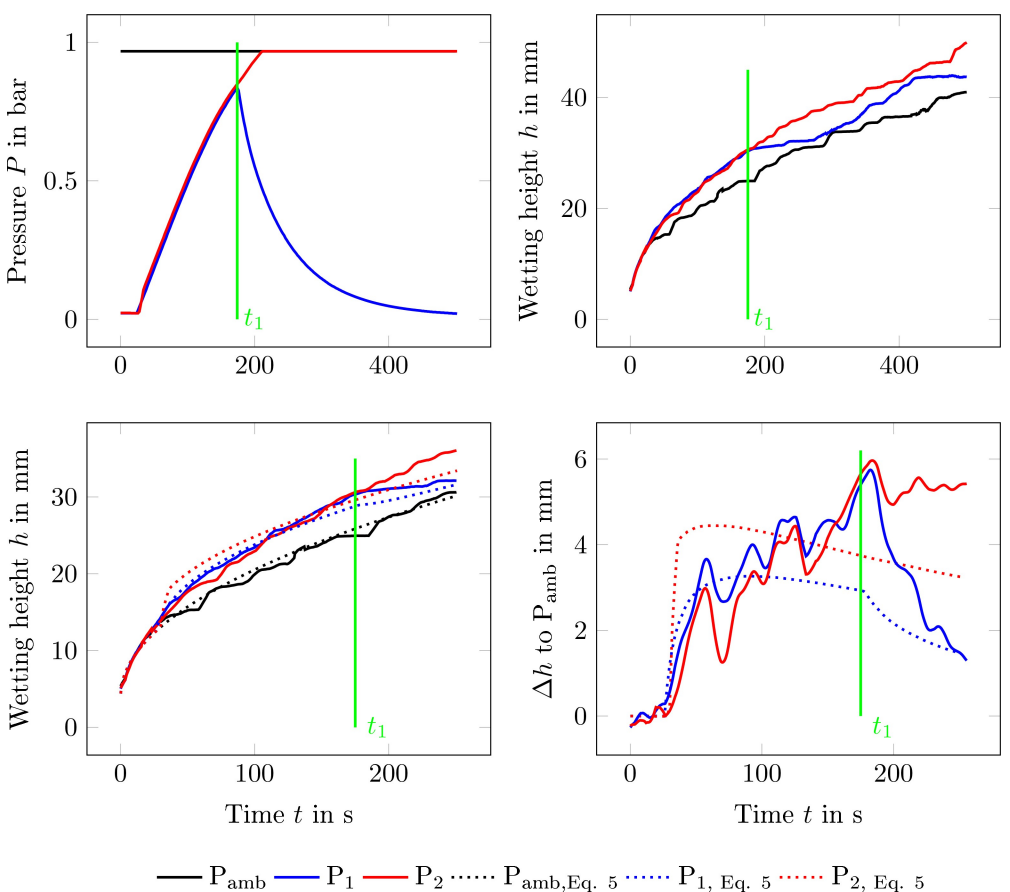


Figure 7. Illustration of the different pressure curves over time in (a) and the resulting experimental wetting height over time in (b). The experimental and calculated wetting heights over time are shown in (c). Figure (d) depicts the difference between the wetting height at varying process pressures and the wetting height at a constant pressure of 968 mbar, both from the experiments and the calculated wetting.

300 s. For $t > 300$ s, the wetting of P_1 increases compared to P_{amb} . Figure 7 (c) presents the experimental wetting curves up to $t = 250$ s along with the calculated wetting curves for each scenario. A good replication of the calculated wetting is particularly evident for P_{amb} and P_1 . Figure 7 (d) illustrates the difference between the wetting height and the reference for both experimental and calculated wetting. There is a clear correlation between the pressure changes at $t = 25$ s for P_1 and P_2 as acceleration when compared to P_{amb} . This correlation is observed both in experimental results and in calculations. At $t = 174$ s, the distance between the wetting heights of P_1 and P_2 decreases in both the experiments and the mathematical replication. Here a relationship between the constant pressure and the pressure decrease on the wetting is observed. If no change in pressure is applied, the wetting process remains consistent for both 968 mbar and 20 mbar pressures. Additionally, variations in surface tension and contact angle have a minimal effect on the wetting level within this short time frame, as observed in the experimental wetting up to $t = 25$ s. Overall, after 500 s, P_2 exhibits a 21.4% faster wetting rate compared to P_{amb} .

Cell Level

In the experiment with a 21700 cell, a vacuum of 100 mbar is selected due to the vapor pressure of the electrolyte. Three ml of electrolyte are injected into the upper edge of the winding core using a syringe. The resulting wetting process is shown in Figure 8. Following the injection, significant foam formation occurs above the cell. Initially, an electrolyte distribution can be registered from the top of the cell and later from the bottom, progressing towards the center, with particular filling observed in the space between the housing and coil. From $t = 30$ s to $t = 90$ s, the ambient pressure increases to 968 mbar, leading to a significant rise in electrolyte volume and a darkening of the separator. At $t = 90$ s, white spots on the separator, particularly in the upper and lower parts, indicate delayed wetting caused by an attached adhesive strip. Between $t = 90$ s and $t = 400$ s, there is a decrease in the filling level between the outer winding and the cell housing, likely due to wetting of the inner windings. Gas entrainment in the lower right-hand area, noted between $t = 20$ s and $t = 200$ s, gradually decreases and is nearly eliminated after $t = 400$ s. In contrast, a reference measurement at ambient pressure shows a similar distribution and electrolyte flow direction but with larger and permanent gas entrainments.

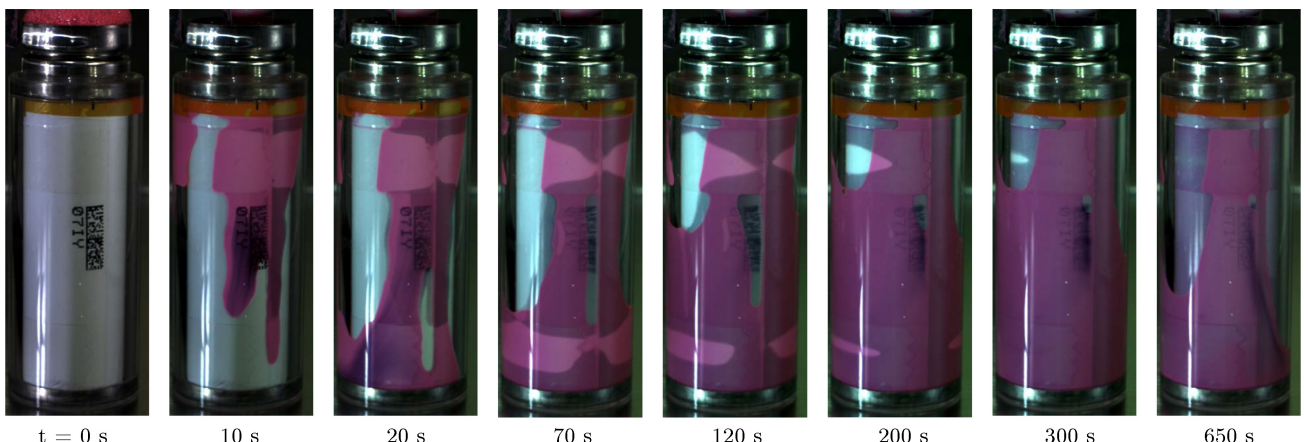


Figure 8. Experimental illustration of the wetting of the cylindrical cell at a negative pressure of 100 mbar. A high-contrast electrolyte is used to wet the NMC Jelly roll. Between 30 s and 90 s the process pressure is changed to 968 mbar.

Unlike material-level experiments, which do not exhibit foam formation, the cell-level experiments show foam and different wetting behavior due to the top and bottom wetting process, resulting in gas entrapments between the outermost winding and the housing. These gas entrapments are not noticeable in material tests due to compression. The influence of varying pressure conditions is more pronounced at the cell level than at the material level. This phenomenon is primarily due to gas entrapment and the dynamic injection process of the electrolyte, as well as the cavities around the jelly roll.

Influence of Overpressure

Based on the experimental results with negative pressure, the effect of positive pressure is investigated using Equation 1. To this end, three different pressure profiles are compared a reference with $P_{\text{amb}}=968$ mbar, a negative pressure of 100 mbar with subsequent overpressure of 6 bar (P_3) and a repeating overpressure cycle between 968 mbar and 6 bar (P_4). The pressure profiles and the resulting wetting heights, based on the anode properties listed Table 1, an assumed porous medium height of 70 mm, and the solvent DMC, are depicted in Figures 9b and 9c.

There is no deviation between the static negative pressure at 100 mbar and the reference at the wetting level up to $t=36$ s. Subsequently, increasing the pressure to 968 mbar up to $t=164$ s, accelerates the wetting compared to the reference. At $t=164$ s, applying an overpressure of 6 bar within 20 s results in a significant increase, in wetting height. After a 36 s holding time, a reducing the pressure to 968 mbar within 20 s decreases the wetting height. Following this, a uniform progression in wetting height is observed at P_3 , gradually approaching the reference level. With repeated pressure variations of P_4 , the same effect is repeatedly observed, although it becomes increasingly weaker as the wetting height progresses. Until $t=600$ s, the distance between the wetting heights of P_4 and P_{amb} is also reduced. At $t=600$ s, overpressure causes a higher wetting of 2.4 mm (P_3 to P_{amb}) and 3.1 mm (P_4 to P_{amb}).

The influence of the ambient pressure on the wetting velocity is also investigated using LBM pore model simulation. For this purpose, wetting of the electrode geometry from Figure 1 is examined under different process pressures based on the pressure curve P_3 . Simulated conditions include pressures of 100 mbar, 500 mbar, 968 mbar, 3 bar, and 6 bar. To this end, the model is parameterized with the contact angle, surface tension, the density difference between liquid and gas, and, if necessary, the pressure difference as described by Equation 4. For dynamic pressure changes, a ∇P_V through the porous medium of 18.5 kPa at 500 mbar and 102 kPa at 3 bar results from the mathematical calculation shown in Figure 9. The resulting deviations in the pressure-saturation behavior are small. The macroscopic velocity of complete wetting for the electrode section is presented in Table 2. The resulting velocities from the lattice Boltzmann pore model simulation range from 44.4 to 46.1 mm/s. The influence of surface tension, contact angle, and density difference between gas and liquid at 0.1, 0.968 and 6 bar is negligible. A static overpressure of 6 bar increases wetting speed by 0.68% compared to 0.968 bar. During dynamic pressure changes, ∇P_V at 500 mbar leads to a wetting speed increase of 0.3–0.4 mm/s compared to 0.1 mbar and 0.968 bar. At 3 bar dynamic pressure increases result in wetting speeds that are 1.7 mm/s faster than at 0.968 bar and 1.4 mm/s faster than at 6 bar. This highlights the slightly positive effect of overpressure and the significant influence of dynamic pressure changes on wetting.

Table 2. Resulting saturation velocities of the pore model based on different pressure boundary conditions.

t	t ₁	t ₂	t ₃	t ₄	t ₅
P in bar	0.1	0.5	0.968	3	6
v in $\frac{\text{mm}}{\text{s}}$	44.5	44.8	44.4	46.1	44.7

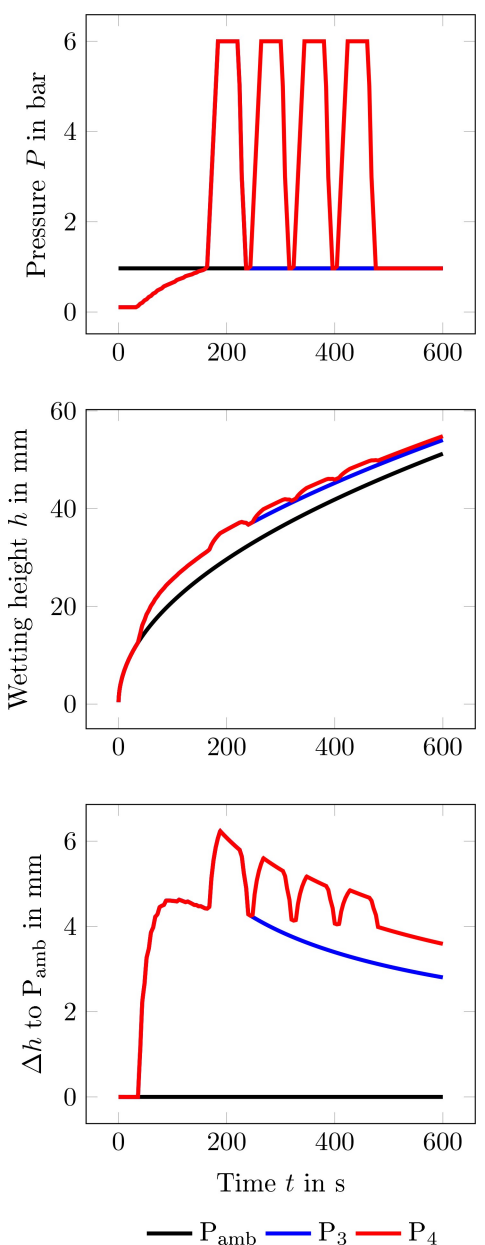


Figure 9. Illustration of the different pressure curves over time in (a) and the resulting calculated wetting height over time in (b). Figure (c) depicts the difference between the wetting height at varying process pressures and the wetting height at a constant pressure of 968 mbar.

Foam Formation During Experiments

The foam formation observed during the injection process in the vacuum tests is particularly crucial due to safety and cleanliness concerns, as splashing electrolyte can be problematic. At a vacuum of 20 mbar, foam is present for 17.5 s in an additional experiment. However, no foam is seen at ambient pressure and a vacuum of 200 mbar during the same injection process. To reduce foaming, the foam stability of the electrolyte can be modified adjusting its temperature. Repeated the experiment at a vacuum of 20 mbar with an electrolyte temper-

ature of -10°C results in a 74% reduction in foam volume, the foam persists for just 3.5 s.

Conclusions and Discussion

The results highlight the benefits of using a transparent cylindrical cell housing for electrolyte filling and the subsequent wetting of a lithium-ion battery cell. Findings from planar material tests on individual electrode materials can be extended to the cell level. Experimental studies under varying temperature and pressure conditions are supported by mathematical modeling and the lattice Boltzmann pore model. Targeted temperature control plays a crucial role in wetting, primarily due to its effect on electrolyte viscosity. Raising the temperature from 5°C to 45°C accelerates wetting by 35%. According to Günter et al., a similar increase in temperature from 20°C to 40°C results in a threefold acceleration of wetting at the cell level.^[16] Davoodabadi et al. report a 3–30% faster electrolyte distribution in the droplet spread tests with temperatures rising from 23°C to 43°C , with variation due to differing electrolytes.^[14] Therefore, results should be tailored to the respective electrolyte or solvent used. The pore model findings support these observations, showing that wetting occurs more efficiently at lower capillary pressures at higher temperatures, with increased mobility of gas entrainment. Therefore, controlled heating of the cell during the wetting process is advisable.

Using static vacuum of 0.02 mbar or 0.1 mbar has little to no effect on wetting, as demonstrated by the experiments, mathematical replication, and the pore model simulations within the static pressure range. However, variations in process pressure do impact the wetting process. Increasing pressure accelerates wetting, while decreasing pressure hinders it. This effect is closely tied to the contact point between the gas and the pore. For instance, a dynamic pressure increase from 20 mbar to 968 mbar leads to 21.4% faster wetting after 500 s compared to reference pressure. Mathematical results also suggest that faster and repetitive pressure changes slightly enhance wetting, a finding confirmed by Knoche et al.^[15] Gas entrainment is visible in the glass cell housing experiments, where a heterogeneous distribution of the electrolyte immediately after filling leads to significant gas entrainment. This observation aligns with literature reports. Pressure experiments and mathematical replications conducted by Günter et al. demonstrate that applying negative pressure reduces gas entrainment and accelerates the wetting process. The impact of cyclic pressure tests is also beneficial, provided that there are no gas entrainments present.^[16] Hagemeister et al. corroborate these findings through pore-scale simulations.^[17] Additionally, the introduction of a dye tracing into the electrolyte enables the detection of foam during electrolyte filling under vacuum conditions due to the injection pressure. However, foam formation can be reduced by targeted cooling of the electrolyte.

The limitations of this method are the focus on the round cell and the view of the outermost winding of the jelly roll. The electrolyte movements in the inner windings cannot be

observed. In addition, the transfer between the simulation and the experiments is only qualitative. For a detailed simulation, a complex cell model could be created that can simulate the filling process with sufficient resolution using significant computing resources.

Furthermore, the use of a glass casing in the experimental setup provides considerable advantages, particularly in process configuration. This approach not only allows precise control over temperature and process pressure but also enables further investigation into additional factors that enhance wetting.

Supporting Information

The LBM pore model simulation utilizes the multicomponent Shan–Chen method. Adhesion parameters $G_{\text{ads}}^{\text{E,G}}$ are determined as described in Ref. [42]. In this simulation, dimethyl carbonate (DMC) serves as the electrolyte, while air is represented as the gas, both at 20°C and ambient pressure. The resulting conversion factors for lattice and SI units are listed in Tables 3 and 4.

Acknowledgements

This research was funded by the Federal Ministry of Education and Research (BMBF), funding code 03XP0529D. The authors would like to express their gratitude to the Federal Ministry of Education and Research, Germany, for funding this work as part of the accompanying research project “VisEl-Visualisierung der Elektrolytbewegungen und Elektrodenausdehnung einer Lithium-Ionen-Zelle”. Open Access funding enabled and organized by Projekt DEAL.

Conflict of Interests

The authors declare no conflict of interest. The funders were not involved in the study's design, data collection, analysis, interpretation, manuscript writing, or decision to publish the results.

Data Availability Statement

The data that support the findings of this study are available from the corresponding author upon reasonable request.

Keywords: lithium-ion battery • electrolyte wetting • 21700 cylindrical cell • lattice Boltzmann method

Table 3. Overview of the physical parametrization of the electrolyte (E) and gas (G).

	SI units	lattice units
Length	$l = 4.59 \cdot 10^{-8} \text{ m}$	$l = 1 \text{ lu}$
Density	$\rho^{\text{E}} = 1070 \frac{\text{kg}}{\text{m}^3}$	$\rho^{\text{E}} = \rho^{\text{G}} = 2 \frac{\text{mu}}{\text{lu}^3}$
	$\rho^{\text{G}} = 1.21 \frac{\text{kg}}{\text{m}^3}$	$\rho_{\text{dis}}^{\text{E}} = \rho_{\text{dis}}^{\text{G}} = 0.06 \frac{\text{mu}}{\text{lu}^3}$
Kinematic viscosity	$\nu^{\text{E}} = 5.88 \cdot 10^{-7} \frac{\text{m}^2}{\text{s}}$	$\nu^{\text{E}} = 1.667 \cdot 10^{-1} \frac{\text{lu}^2}{\text{ts}}$
	$\nu^{\text{G}} = 1.57 \cdot 10^{-5} \frac{\text{m}^2}{\text{s}}$	$\nu^{\text{G}} = 1.667 \cdot 10^{-1} \frac{\text{lu}^2}{\text{ts}}$
Surface tension	$\gamma = 2.91 \cdot 10^{-2} \frac{\text{kg}}{\text{s}^2}$	$\gamma = 4.22 \cdot 10^{-3} \frac{\text{mu}}{\text{ts}^2}$
Contact angle	$\theta = 14.8^\circ$	$G_{\text{inter}}^{\text{EG}} = G_{\text{inter}}^{\text{GE}} = 0.9$
		$G_{\text{ads}}^{\text{G}} = -G_{\text{ads}}^{\text{E}} = 0.422$
Relaxation coefficient		$\tau^{\text{E}} = \tau^{\text{G}} = 1$

Table 4. Conversion factors between SI units and LBM units (lu= length unit, ts = time step, mu = mass unit).

Unit	Conversion factor
Length	$C_l = 4.59 \cdot 10^{-8} \frac{\text{m}}{\text{lu}}$
Time	$C_t = 5.97 \cdot 10^{-10} \frac{\text{s}}{\text{ts}}$
Mass	$C_m = 5.17 \cdot 10^{-20} \frac{\text{kg}}{\text{mu}}$
Pressure	$C_p = 3.16 \cdot 10^6 \frac{\text{kg/m/s}^2}{\text{mu/lu/ts}^2}$
Kinematic viscosity	$C_v = 3.53 \cdot 10^{-6} \frac{\text{m}^2/\text{s}}{\text{lu}^2/\text{ts}}$
Force density	$C_f = 1.29 \cdot 10^{11} \frac{\text{m/s}^2}{\text{lu}/\text{ts}^2}$
Dynamic viscosity	$C_d = 1.89 \cdot 10^{-3} \frac{\text{kg/m/s}}{\text{mu/lu/ts}}$
Velocity	$C_u = 7.69 \cdot 10^1 \frac{\text{m/s}}{\text{lu/ts}}$
Surface tension	$C_s = 1.45 \cdot 10^{-1} \frac{\text{kg/s}^2}{\text{mu/lu}^2}$

- [1] J. Full, J. Wanner, S. Kiemel, R. Miehe, M. Weeber, A. Sauer, Comparing Technical Criteria of Various Lithium-Ion Battery Cell Formats for Deriving Respective Market Potentials, in *2020 IEEE Electric Power and Energy Conference (EPEC)*, IEEE, Piscataway, NJ 2020 pages 1–6.
- [2] S. Baaouzi, N. Feistel, J. Wanner, I. Landwehr, A. Fill, K. P. Birke, *Batteries* **2023**, 9, 309.
- [3] M. Weeber, J. Wanner, P. Schlegel, K. P. Birke, A. Sauer, *Proc. Manuf.* **2020**, 43, 32.
- [4] A. Kwade, W. Haselrieder, R. Leithoff, A. Modlinger, F. Dietrich, K. Droeder, *Nat. Energy* **2018**, 3, 290.
- [5] J. Wanner, M. Weeber, K. P. Birke, A. Sauer, *Procedia CIRP* **2022**, 112, 507.
- [6] A. Kampker, H. Heimes, C. Offermanns, S. Wennemar, T. Robben, N. Lackner, *WEV* **2023**, 14, 96.
- [7] J. Wanner, M. Weeber, K. P. Birke, A. Sauer, *Procedia CIRP* **2023**, 118, 987.
- [8] L. Gold, T. Herzog, F. Schubert, H. Heuer, G. A. Giffin, *Energy Technol.* **2023**, 11, 2200861.
- [9] A. Schilling, P. Gümbel, M. Möller, F. Kalkan, F. Dietrich, K. Dröder, *J. Electrochem. Soc.* **2019**, 166, A5163.
- [10] J. Wanner, K. P. Birke, *J. Energy Storage* **2024**, 87, 111410.
- [11] J. Wanner, M. Weeber, K. P. Birke, A. Sauer, Quality Modelling in Battery Cell Manufacturing Using Soft Sensing and Sensor Fusion A Review, in *2019 9th International Electric Drives Production Conference (E/DPC)*, IEEE, Piscataway, NJ 2019 pages 1–9.
- [12] N. Kaden, R. Schlüter, A. Rohde Garcfa, K. Dröder, *Batteries* **2023**, 9, 164.
- [13] N. Kaden, N. Schlüter, R. Leithoff, S. Savas, S. Grundmeier, K. Dröder, *Processes* **2021**, 9, 1851.
- [14] A. Davoodabadi, J. Li, H. Zhou, D. L. Wood, T. J. Singler, C. Jin, *J. Energy Storage* **2019**, 26, 101034.
- [15] T. Knoche, V. Zinth, M. Schulz, J. Schnell, R. Gilles, G. Reinhart, *J. Power Sources* **2016**, 331, 267.
- [16] F. J. Günter, J. Keilhofer, C. Rauch, S. Rössler, M. Schulz, W. Braunwarth, R. Gilles, R. Daub, G. Reinhart, *J. Power Sources* **2022**, 517, 230668.
- [17] J. Hagemeister, F. J. Günter, T. Rinner, F. Zhu, A. Papst, R. Daub, *Batteries* **2022**, 8, 159.
- [18] S. G. Lee, D. H. Jeon, *J. Power Sources* **2014**, 265, 363.
- [19] D. H. Jeon, *Energy Storage Mater.* **2019**, 18, 139.

- [20] A. Shodiev, E. Primo, O. Arcelus, M. Chouchane, M. Osenberg, A. Hilger, I. Manke, J. Li, A. A. Franco, *Energy Storage Mater.* **2021**, *38*, 80.
- [21] D. H. Jeon, J.-H. Song, J. Yun, J.-W. Lee, *ACS Nano* **2023**, *17* (2), 1305–1314.
- [22] M. Abubaker, C.-H. Sohn, H. M. Ali, *J. Therm. Anal. Calorim.* **2024**, *149*, 5443.
- [23] M. P. Lautenschlaeger, B. Prifling, B. Kellers, J. Weinmiller, T. Danner, V. Schmidt, A. Latz, *Batteries & Supercaps* **2022**, *5*, e202200090.
- [24] C. Sauter, R. Zahn, V. Wood, *J. Electrochem. Soc.* **2020**, *167*, 100546.
- [25] J. Wanner, K. P. Birke, *Batteries* **2022**, *8*, 277.
- [26] J. Hagemeyer, S. Stock, M. Linke, M. Fischer, R. Drees, M. Kurrat, R. Daub, *Energy Technol.* **2023**, *11*, 2200686.
- [27] E. W. Washburn, *Phys. Rev.* **1921**, *17*, 273.
- [28] N. Fries, M. Dreyer, *J. Colloid Interface Sci.* **2008**, *320*, 259.
- [29] J. Wanner, K. P. Birke, *Energies* **2023**, *16*, 5640.
- [30] E. W. Lemmon, *J. Phys. Chem. Ref. Data* **2011**, *40*, 043106.
- [31] A. Rodríguez, J. Canosa, A. Domínguez, J. Tojo, *J. Chem. Eng. Data* **2003**, *48*, 146.
- [32] Merck KGaA, 803525 Sigma-Aldrich Dimethylcar-bonat: Dimethyl carbonate for synthesis. CAS 616-38-6, chemical formula $(\text{CH}_3\text{O})_2\text{CO}$ **2022**.
- [33] Merck KGaA, 310328 310328 – Sigma-Aldrich Propyencarbonat **2024**.
- [34] J. Latt, O. Malaspinas, D. Kontaxakis, A. Parmigiani, D. Lagrava, F. Brogi, M. B. Belgacem, Y. Thorimbert, S. Leclaire, S. Li, F. Marson, J. Lemus, C. Kotsalos, R. Conradi, C. Coreixas, R. Petkantchin, F. Raynaud, J. Beny, B. Chopard, *C and M with Applications* **2021**, *81*, 334.
- [35] S. Chen, *Phys Rev E Stat Phys Plasmas Fluids Relat Interdiscip Topics* **1993**, *47*, 1815.
- [36] Q. Lou, Y. Yan, H. Xu, *J. Appl. Phys.* **2022**, *132*.
- [37] J. Hua, J. Lou, *J. Comput. Phys.* **2007**, *222*, 769.
- [38] F. Wang, J. Wu, Z. Liu, *Fluid Phase Equilib.* **2004**, *220*, 123.
- [39] J. Li, P. Meng, H. Zhou, *Ionics* **2018**, *24*, 2147.
- [40] J.-W. Song, L.-W. Fan, *Adv. Colloid Interface Sci.* **2021**, *288*, 102339.
- [41] W. Sachs, V. Meyn, *Colloids Surf. A* **1995**, *94*, 291.
- [42] H. Huang, D. T. Thorne, M. G. Schaap, M. C. Sukop, *Phys Rev E Stat Nonlin Soft Matter Phys* **2007**, *76*, 066701.

Manuscript received: August 6, 2024

Revised manuscript received: October 7, 2024

Accepted manuscript online: October 8, 2024

Version of record online: November 16, 2024